Pathophysiological interplay between *O*-GlcNAc transferase and the Machado–Joseph disease protein ataxin-3

Priscila Pereira Sena[a,b,c], Jonasz J. Weber[a,b,d], Maxinne Watchon[e], Katherine J. Robinson[e], Zinah Wassouf[a,b,1], Stefan Hauser[f,g], Jacob Helm[f,g], Mahkameh Abeditashi[a,b,c], Jana Schmidt[a,b], Jeannette Hübener-Schmid[a,b], Ludger Schöls[f,g], Angela S. Laird[e], Olaf Riess[a,b], and Thorsten Schmidt[a,b,2]

[a]Institute of Medical Genetics and Applied Genomics, University of Tübingen, Tübingen 72076, Germany; [b]Center for Rare Diseases, University of Tübingen, Tübingen 72076, Germany; [c]Graduate School of Cellular Neuroscience, University of Tübingen, Tübingen 72074, Germany; [d]Department of Human Genetics, Ruhr-University Bochum, Bochum 44801, Germany; [e]Centre for Motor Neuron Disease Research, Macquarie Medical School, Faculty of Medicine, Health and Human Sciences, Macquarie University, Sydney, NSW 2109, Australia; [f]German Center for Neurodegenerative Diseases, Tübingen 72076, Germany; and [g]Department of Neurology, Hertie Institute for Clinical Brain Research, University of Tübingen, Tübingen 72076, Germany

Edited by Huda Y. Zoghbi, Baylor College of Medicine, Houston, TX, and approved October 15, 2021 (received for review January 6, 2021)

Aberrant *O*-GlcNAcylation, a protein posttranslational modification defined by the *O*-linked attachment of the monosaccharide *N*-acetylglucosamine (*O*-GlcNAc), has been implicated in neurodegenerative diseases. However, although many neuronal proteins are substrates for *O*-GlcNAcylation, this process has not been extensively investigated in polyglutamine disorders. We aimed to evaluate the enzyme *O*-GlcNAc transferase (OGT), which attaches *O*-GlcNAc to target proteins, in Machado–Joseph disease (MJD). MJD is a neurodegenerative condition characterized by ataxia and caused by the expansion of a polyglutamine stretch within the deubiquitinase ataxin-3, which then present increased propensity to aggregate. By analyzing MJD cell and animal models, we provide evidence that OGT is dysregulated in MJD, therefore compromising the *O*-GlcNAc cycle. Moreover, we demonstrate that wild-type ataxin-3 modulates OGT protein levels in a proteasome-dependent manner, and we present OGT as a substrate for ataxin-3. Targeting OGT levels and activity reduced ataxin-3 aggregates, improved protein clearance and cell viability, and alleviated motor impairment reminiscent of ataxia of MJD patients in zebrafish model of the disease. Taken together, our results point to a direct interaction between OGT and ataxin-3 in health and disease and propose the *O*-GlcNAc cycle as a promising target for the development of therapeutics in the yet incurable MJD.

ataxin-3 | Machado–Joseph disease | Spinocerebellar ataxia type 3 | O-GlcNAc | OGT

Many neurodegenerative conditions present disturbances in brain glucose uptake as a common factor (1). The *O*-glycosidically linked monosaccharide *N*-acetylglucosamine (*O*-GlcNAc), discovered as a posttranslational modification (PTM) termed *O*-GlcNAcylation (2), represents a potential link between dysfunctional brain glucose metabolism and neurodegeneration.

The enzyme *O*-GlcNAc transferase (OGT) (3) attaches *O*-GlcNAc to target proteins, whereas its removal from a protein is catalyzed by the enzyme *O*-GlcNAcase (OGA) (4). As a highly dynamic and abundant PTM, *O*-GlcNAcylation is shown to contribute to the pathophysiology of Alzheimer's disease (AD) (5), Parkinson's disease (PD) (6), and the polyglutamine (polyQ) disorder Huntington's disease (HD) (7), possibly competing with phosphorylation for modulating protein activity (8). Several neuronal key proteins were shown to interact with OGT (9, 10); however, for polyQ proteins involved in neurodegeneration, a limited number of studies are available (7, 11).

To further understand the conceivable connection between *O*-GlcNAcylation and polyQ disorders, we evaluated this PTM and its enzyme OGT in Machado–Joseph disease (MJD), also known as spinocerebellar ataxia type 3, the most common autosomal dominant ataxia worldwide (12). MJD is caused by an elongated polyQ stretch within the deubiquitinase (DUB) ataxin-3 (13), resulting in perturbed interactions and increased aggregation propensity of the polyQ-expanded protein (14, 15). Some metabolic changes in MJD patients point to disturbances in glucose utilization (16, 17), but *O*-GlcNAcylation has yet not been investigated. A study demonstrated that moderate caloric restriction improved motor coordination in MJD mouse models via sirtuin-1 (18), an enzyme modulated by *O*-GlcNAcylation (19). Furthermore, *O*-GlcNAcylation was shown to impact autophagy (20, 21), a protein degradation pathway dysregulated in MJD (22, 23) and recognized as a potential therapeutic target for neurodegenerative diseases (24, 25). In models of HD, lowering global *O*-GlcNAcylation resulted in enhanced autophagic flux, less protein aggregation, and reduced polyQ toxicity (26).

Significance

Machado–Joseph disease (MJD) is an incurable neurodegenerative disorder caused by a mutation in the ataxin-3 protein, which becomes toxic and induces cerebellar degeneration and motor impairments. Disturbances in the protein modification *O*-GlcNAcylation, catalyzed by the enzyme *O*-GlcNAc transferase (OGT), have been linked to neurodegeneration, but its potential involvement in MJD remains elusive. By analyzing MJD cells and animal models, we demonstrate altered levels of OGT in MJD, further identifying this enzyme as a substrate of ataxin-3. Targeting OGT reduced ataxin-3 toxicity, improving the motor phenotype of an MJD animal model. Our results unveiled a physiological interplay between ataxin-3 and OGT, highlighting OGT as a potential therapeutic target in this deadly condition.

Author contributions: P.P.S., J.J.W., M.W., S.H., O.R., and T.S. designed research; P.P.S., J.J.W., M.W., K.J.R., Z.W., J.H., M.A., J.S., and J.H.-S. performed research; S.H., L.S., A.S.L., O.R., and T.S. contributed new reagents/analytic tools; P.P.S., J.J.W., M.W., K.J.R., Z.W., and A.S.L. analyzed data; P.P.S. and J.J.W. wrote the paper; J.S. and J.H.-S. provided animal samples; and L.S. provided human fibroblasts.

The authors declare no competing interest.

This article is a PNAS Direct Submission.

[1]Present address: Wellcome Sanger Institute, Wellcome Genome Campus, Hinxton, Cambridge CB10 1SA, UK.

[2]To whom correspondence may be addressed. Email: Thorsten.Schmidt@med.uni-tuebingen.de.

This article contains supporting information online at http://www.pnas.org/lookup/suppl/doi:10.1073/pnas.2025810118/-/DCSupplemental.

Published November 16, 2021.

Here, we show that OGT is elevated in cells, transgenic mice, and zebrafish models of MJD. We demonstrate that ataxin-3 is a regulator of OGT protein levels and ubiquitination status, likely contributing to the control of autophagy. Furthermore, genetic and pharmacological modulation of OGT levels and activity reduced soluble and aggregated forms of polyQ-expanded ataxin-3 in cell and zebrafish MJD models, resulting in increased viability and improved motor function, respectively. Our study sheds light on a physiological role of ataxin-3 and helps to evaluate whether targeting OGT and therefore *O*-GlcNAcylation is a prudent strategy for MJD treatment.

Results

OGT Level Is Increased in Cell and Animal Models of MJD. *O*-GlcNAc cycling is known to be compromised in the pathophysiology of diverse neurodegenerative disorders (27). For instance, postmortem brains of PD patients presented increased *O*-GlcNAcylation in the temporal cortex (28). Since OGT is the sole enzyme mediating the attachment of *O*-GlcNAc moieties, we investigated whether OGT levels are altered in MJD. We first analyzed ataxin-3 knockout human embryonic kidney (HEK) 293T cells (293T *ATXN3*$^{-/-}$), transiently transfected with constructs expressing wild-type ataxin-3 with 15 glutamines (15Q) or polyQ-expanded ataxin-3 with 148 glutamines (148Q). Western blot analysis revealed increased OGT protein level in cells expressing polyQ-expanded ataxin-3 (Fig. 1*A*). To confirm this finding in MJD cellular models expressing endogenous polyQ-expanded ataxin-3, we analyzed protein extracts from SV40 immortalized patient-derived fibroblasts (IHF) and induced pluripotent stem cell (iPSC)–derived cortical neurons (iCN) originated from MJD patients. Western blot analysis also revealed an increase of OGT in the MJD patient-derived samples (Fig. 1 *B* and *C*). Cortical lysates of 5-mo-old transgenic MJD mice (MJD) also presented increased OGT levels at baseline (Fig. 1*D*). Furthermore, we confirmed increased global *O*-GlcNAcylation in transfected cells expressing polyQ-expanded ataxin-3 and in MJD patient-derived IHF as a result of the high OGT levels (*SI Appendix*, Fig. S1 A and B).

Ataxin-3 Regulates OGT Protein Levels. As demonstrated in Fig.1, various MJD models presented increased levels of OGT, an enzyme previously shown to be a substrate for the ubiquitin proteasome system (UPS) (29). As a DUB, ataxin-3 might modify ubiquitin chains attached to OGT, thereby influencing its clearance. Thus, we tested whether the presence or absence of wild-type ataxin-3 directly modulates OGT levels. Protein extracts from 293T *ATXN3*$^{-/-}$ cells and cerebellar lysates of 11-mo-old ataxin-3 knockout (*Atxn3*$^{-/-}$) mice (30) were analyzed for baseline OGT protein levels. 293T *ATXN3*$^{-/-}$ cells had decreased amount of OGT protein and decreased global *O*-GlcNAcylation, as shown by Western blot analysis (Fig. 2 *A* and *B*, respectively). OGT protein level was also reduced in samples of *Atxn3*$^{-/-}$ mice (Fig. 2*C*), supporting our hypothesis that wild-type ataxin-3 acts as a regulator of OGT. Further, we performed a cycloheximide (CHX) chase assay in order to analyze OGT stability in presence or absence of ataxin-3. Total ubiquitin (Ub) chains reduced over time in cells treated with CHX and were used as positive control (Fig. 2*D*). OGT presented lower stability in 293T *ATXN3*$^{-/-}$ cells (Fig. 2*E*), pointing toward a shorter half-life of OGT in the absence of ataxin-3. Transient expression of wild-type ataxin-3 (Atx3 15Q) in 293T *ATXN3*$^{-/-}$ cells restored OGT protein level (Fig. 2*F*). In order to assess whether the modulation of OGT levels by ataxin-3 resulted from differences in its gene transcription, we compared OGT messenger ribonucleic acid (mRNA) expression in wild-type 293T versus 293T *ATXN3*$^{-/-}$ cells and 293T *ATXN3*$^{-/-}$ cells versus cells transfected with ataxin-3 15Q. Analysis via qRT-PCR detected no changes in OGT mRNA expression in both comparisons (Fig. 2 *G* and *H*, respectively), indicating that the modulation of OGT by ataxin-3 occurs at the protein level.

Ataxin-3 Modulates Ubiquitinated OGT. It was evident that OGT is reduced and less stable in ataxin-3 knockout cells and

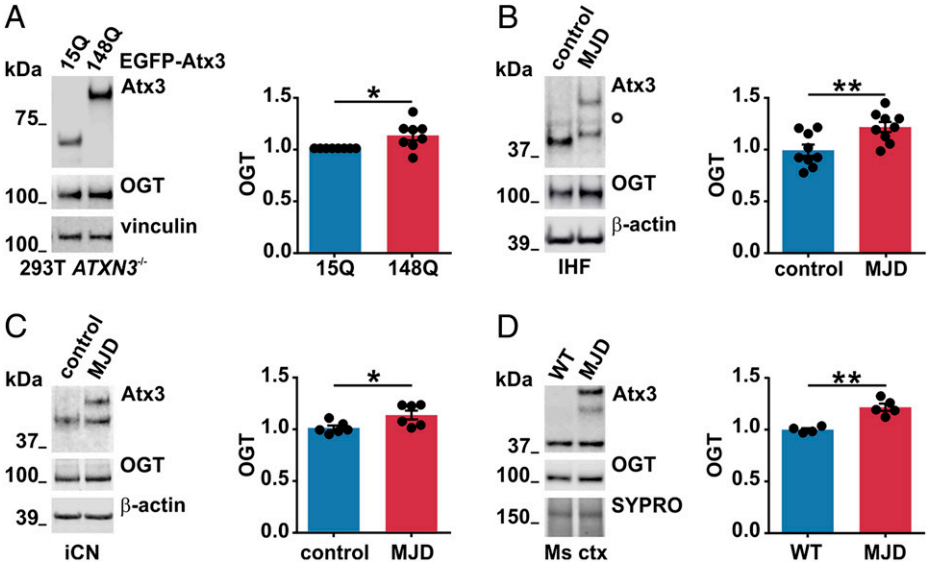

Fig. 1. Increased OGT levels in various models of MJD. (*A*) Western blot analysis of samples from ataxin-3 knockout HEK 293T cells (293T *ATXN3*$^{-/-}$) expressing EGFP-tagged wild-type (15Q) or polyQ-expanded (148Q) ataxin-3 revealed increased OGT levels in cells expressing ataxin-3 148Q. Vinculin served as loading control. $n = 8$, one-sample *t* test, and $P = 0.032$. (*B*) Western blot analysis of different batches of IHF of an MJD patient and a matched control demonstrated increased OGT in MJD samples. White bullet sign (^) indicates unspecific bands, and β-actin served as loading control. $n = 9$, unpaired *t* test, and $P = 0.007$. (*C*) Western blot analysis of two independent batches of iCN from three MJD patients versus three controls revealed increased levels of OGT in patient-derived iCN. β-actin served as loading control. $n = 6$, unpaired *t* test, and $P = 0.029$. (*D*) Western blot analysis of mouse cortical samples (Ms ctx) from 5-mo-old wild-type (WT) and CamKII/MJD77 transgenic mice (MJD) demonstrated increased OGT levels in MJD mice. SYPRO Ruby staining served as loading control. $n = 4$ to 5, unpaired *t* test, and $P = 0.001$. Data are represented as means ± SEM, $^*P \leq 0.05$ and $^{**}P \leq 0.01$.

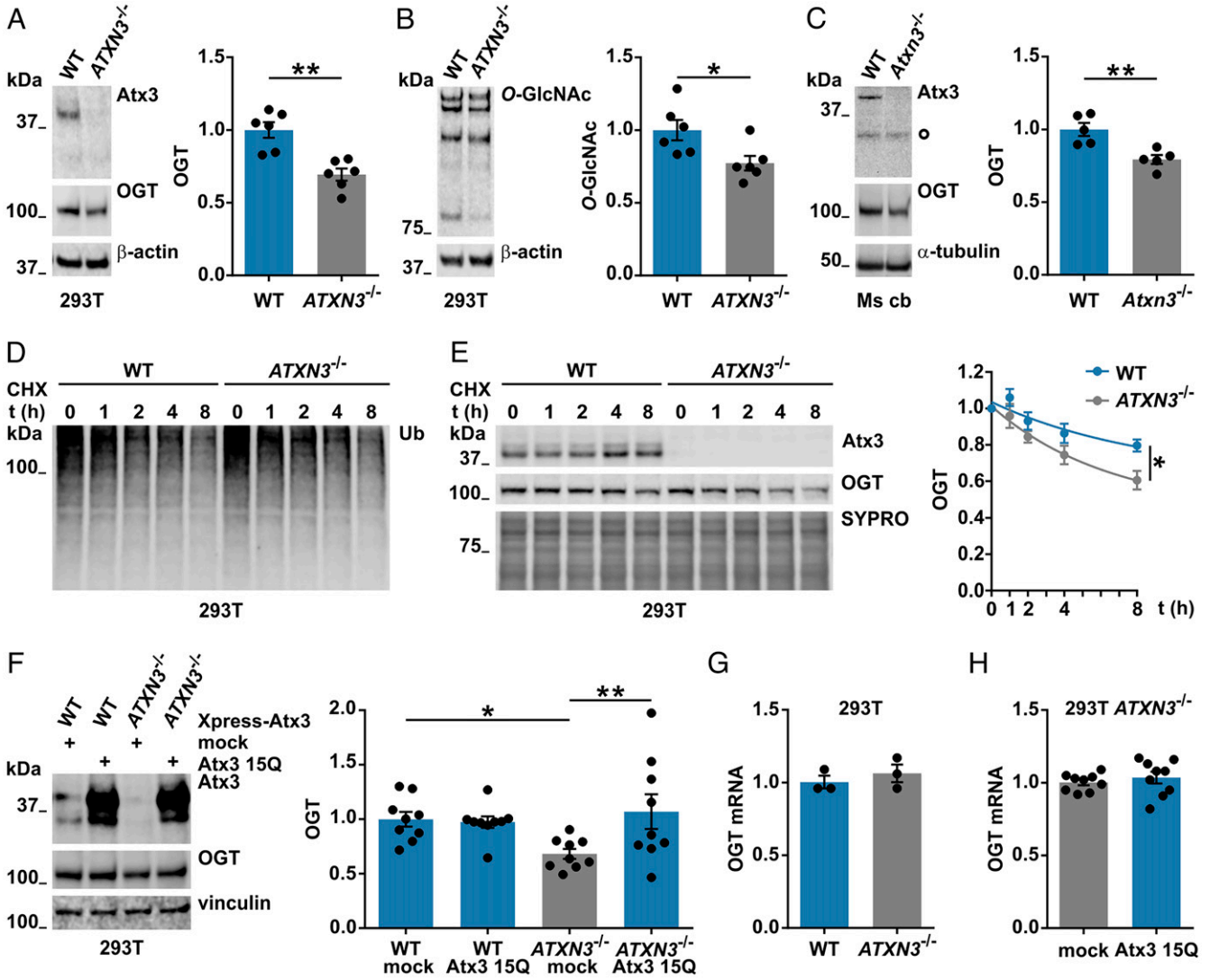

Fig. 2. Wild-type ataxin-3 regulates OGT levels. (*A* and *B*) Western blot analysis of wild-type (WT) and ataxin-3 knockout ($ATXN3^{-/-}$) 293T samples for assessing baseline OGT levels. Comparison showed decreased OGT (*A*) and decreased global *O*-GlcNAc (*B*) in 293T $ATXN3^{-/-}$ cells. β-actin served as loading control. (*A*) $n = 6$, unpaired *t* test, and $P = 0.001$; (*B*), $n = 6$, unpaired *t* test, and $P = 0.025$. (*C*) Western blot of cerebellar lysates from 11-mo-old mice showed decreased OGT levels in the cerebellum (Ms cb) of ataxin-3 knockout ($Atxn3^{-/-}$) mice compared to WT animals. White bullet sign (^) indicates unspecific bands. $n = 5$, unpaired *t* test, and $P = 0.005$. (*D*) Time-dependent reduction of Ub chains in cells treated with 25 μM of CHX for assessing OGT degradation in presence or absence of ataxin-3. (*E*) Western blot depicting an increased degradation of OGT in 293T $ATXN3^{-/-}$ compared to WT cells. SYPRO staining served as loading control. $n = 3$, one phase decay, and $P = 0.005$ (rejected null hypothesis that one curve fits both datasets). WT versus $ATXN3^{-/-}$ 8 h, unpaired *t* test, and $P = 0.037$. (*F*) Analysis of samples from WT and 293T $ATXN3^{-/-}$ cells transfected with control (mock) or Xpress-tagged wild-type ataxin-3 (Atx3 15Q) vectors revealed a rescue of OGT protein levels in 293T $ATXN3^{-/-}$cells transfected with ataxin-3 15Q. $n = 9$, two-way ANOVA with Fisher's Least Significant Difference (LSD) post hoc analysis, WT mock versus $ATXN3^{-/-}$ mock, $P = 0.022$; $ATXN3^{-/-}$ mock versus $ATXN3^{-/-}$ 15Q, $P = 0.006$. (*G* and *H*) qRT-PCR for OGT gene expression presented no differences in OGT mRNA levels between the investigated genotypes. *G*, $n = 3$, and 293T WT versus $ATXN3^{-/-}$; *H*, $n = 9$, and 293T $ATXN3^{-/-}$ mock versus $ATXN3^{-/-}$ 15Q. Data are represented as mean ± SEM, $*P \leq 0.05$ and $**P \leq 0.01$.

ataxin-3 expression rescued OGT protein levels. Knowing that ataxin-3 is a DUB, we further aimed at checking the accumulation of ubiquitinated OGT upon inhibition of the UPS in cells lacking ataxin-3. Analysis of protein extracts from wild-type 293T versus 293T $ATXN3^{-/-}$ cells treated with the proteasome inhibitor MG132 demonstrated an accumulation of the proteasomal degradation–associated K48-linked ubiquitin chains in MG132-treated cells (Fig. 3*A*), together with accumulation of full-length and high–molecular weight OGT bands, which we interpreted as ubiquitinated OGT (Fig. 3*B*, Ub OGT, black arrowheads). Ub OGT presented at higher levels in 293T $ATXN3^{-/-}$ cells, pointing to elevated levels of ubiquitinated OGT in cells lacking ataxin-3.

Assuming that OGT could be a substrate for the DUB activity of ataxin-3, we performed deubiquitination assays by incubating lysates of 293T $ATXN3^{-/-}$ cells and control versus MJD IHF with purified His-tagged ataxin-3 (His_6-Atx3) for 30, 60, and 120 min. Western blotting of the DUB assay with 293T $ATXN3^{-/-}$ cell lysates probed for p53, a known substrate for ataxin-3 (31), confirmed the reduction of ubiquitinated forms of this protein (*SI Appendix*, Fig S2B). Moreover, we observed a global reduction of K48- and K63-linked ubiquitin chains (Fig. 3*C*, Ub-K48 and *SI Appendix*, Fig. S2C, Ub-K63, respectively) in this cell line. High–molecular weight OGT bands were also reduced in all three analyzed cell lines (Fig. 3*C* and *SI Appendix*, Fig. S2 A, E, and F, Ub OGT, black arrowheads),

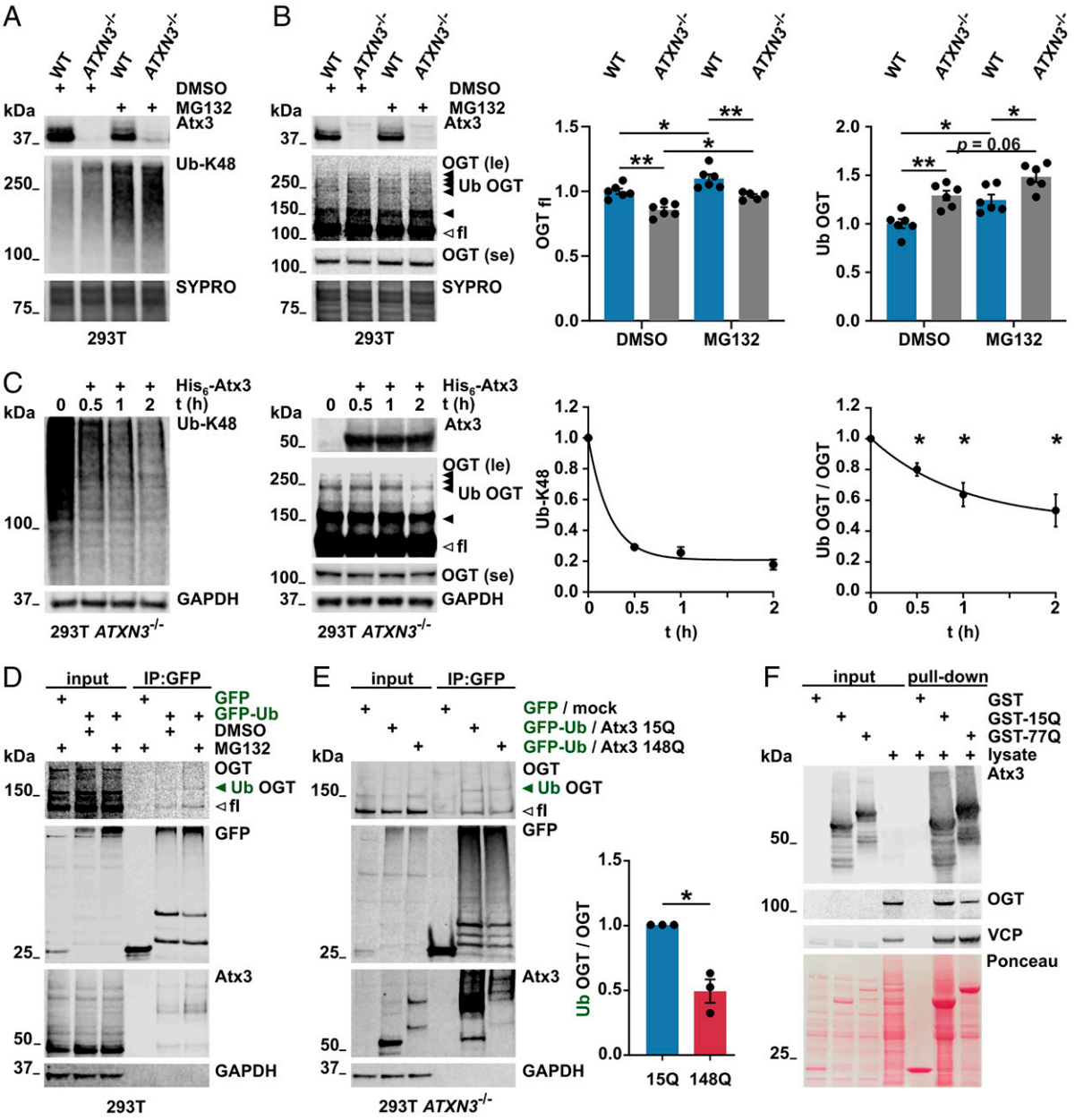

Fig. 3. Ubiquitinated OGT is modulated by ataxin-3. (*A* and *B*) Western blot of wild-type (WT) and ataxin-3 knockout ($ATXN3^{-/-}$) 293T samples. Cells were incubated with DMSO or 10 μM of the proteasome inhibitor MG132 for 4 h prior to harvesting. Proteasome inhibition resulted in increased K48-linked ubiquitin chains (*A*) and increased full-length (unfilled arrowhead) and high–molecular weight OGT bands (*B*), interpreted as ubiquitinated OGT (Ub OGT, black arrowheads). 293T $ATXN3^{-/-}$ cells revealed stronger accumulation of Ub OGT. SYPRO Ruby staining served as loading control. fl = full-length; le = long exposure; and se = short exposure. $n = 6$, one-way ANOVA with Sidak's post hoc analysis. OGT_{fl} in WT DMSO versus $ATXN3^{-/-}$ DMSO, $P = 0.001$; in WT DMSO versus MG132, $P = 0.029$; in $ATXN3^{-/-}$ DMSO versus MG132, $P = 0.022$; in WT MG132 versus $ATXN3^{-/-}$ MG132, $P = 0.004$; Ub OGT in WT DMSO versus $ATXN3^{-/-}$ DMSO, $P = 0.003$; in WT DMSO versus MG132, $P = 0.013$; and in WT MG132 versus $ATXN3^{-/-}$ MG132, $P = 0.016$. (*C*) Western blot of deubiquitination assay. Incubation of 293T $ATXN3^{-/-}$ cell lysates with purified His_6-Atx3 resulted in decreased K48-linked ubiquitin chains (Ub-K48) and decreased levels of Ub OGT (black arrowheads) over time. Full-length OGT (unfilled arrowhead) remained unchanged. GAPDH served as loading control. $n = 3$ to 4, one-sample *t* test, and Ub OGT in 30, 60, and 120 min incubation with His_6-Atx3, $P = 0.018$, $P = 0.018$, and $P = 0.021$ respectively. (*D*) Western blot of immunoprecipitated GFP and GFP-Ub, probed for OGT. GFP constructs were expressed in WT 293T cells for further lysis and immunoprecipitation (IP) of GFP. Cells were incubated with DMSO or 10 μM MG132 for 4 h prior to lysis. IP of GFP-Ub showed increased full-length and high–molecular weight OGT (Ub OGT, green arrowhead) in cells treated with MG132. Ataxin-3 was used as positive control for GFP-Ub–positive proteins. GAPDH served as loading control. le = long exposure and se = short exposure. (*E*) Western blot of immunoprecipitated GFP and GFP-Ub from cells expressing Atx3 15Q or 148Q for analyzing Ub OGT. 293T $ATXN3^{-/-}$ cells were transfected with GFP/empty vector (mock) or GFP-Ub/Atx3 (15Q or 148Q) and treated with 10 μM MG132 for 4 h prior to lysis. IP of GFP probed for OGT confirmed the presence of full-length and Ub OGT (green arrowhead) among GFP-Ub–positive proteins. Ub OGT band was weaker in the IP from cells expressing Atx3 148Q. Ataxin-3 was used as positive control for GFP-Ub–positive proteins. GAPDH served as loading control. $n = 3$, one-sample *t* test, and $P = 0.029$. (*F*) GST pull-down assay for analyzing interaction between ataxin-3 and OGT. GST-tagged WT (GST-15Q) and polyQ-expanded (GST-77Q) ataxin-3 were isolated and incubated with 293T cell lysates. Western blot analysis revealed interaction of both ataxin-3 variants with OGT. GST empty vector was used as negative control for protein interaction and the valosin-containing protein (VCP) was employed as positive control. Total protein was stained with Ponceau S. Data are represented as means ± SEM, $*P \leq 0.05$, and $**P \leq 0.01$.

confirming that the high–molecular weight OGT bands in Fig. 3*B* (black arrowheads) were ubiquitinated forms of OGT. Interestingly, baseline Ub OGT level was reduced in the MJD IHF (*SI Appendix*, Fig. S2F). Our DUB assay thus provided evidence that OGT is a substrate for ataxin-3. Finally, we also observed that ataxin-3 gradually processed more K48- than K63-linked Ub chains (*SI Appendix*, Fig. S2D).

In order to further assess the ubiquitination of OGT, we aimed at precipitating Ub OGT. For this, wild-type 293T cells were transfected with a GFP-tagged ubiquitin (GFP-Ub) construct (32) or its respective control vector (GFP), followed by treatment with the proteasomal inhibitor MG132, for immunoprecipitation of GFP. Western blot analysis revealed that OGT is detectable among GFP-Ub-positive proteins (Fig. 3*D*) and that inhibition of the UPS resulted in increased precipitation of a high–molecular weight, GFP-Ub-positive OGT band (Fig. 3*D*, Ub OGT, green arrowhead).

OGT was increased in presence of polyQ-expanded ataxin-3 (Fig. 1) and ataxin-3 deubiquitinates OGT (Fig. 3*C*). Since Ub OGT was reduced at baseline in MJD IHF (*SI Appendix*, Fig. S2F), we hypothesized that polyQ-expanded ataxin-3 deubiquitinates OGT to a larger extent than wild-type ataxin-3 [as previously reported for parkin (33) and p53 (31)], thus rescuing OGT from proteasomal degradation and promoting its further accumulation in cells expressing polyQ-expanded ataxin-3. In this context, we analyzed Ub OGT in 293T *ATXN3*$^{-/-}$ cells transfected with GFP-Ub and either wild-type (Atx3 15Q) or polyQ-expanded (Atx3 148Q) ataxin-3. The GFP immunoprecipitation probed for OGT revealed the same Ub OGT band observed in Fig. 3*D*, which was weaker in GFP-Ub cotransfected with Atx3 148Q (Fig. 3*E*, green arrowhead), suggesting a stronger DUB activity of polyQ-expanded ataxin-3 toward OGT.

Finally, we investigated a likely direct interaction between OGT and ataxin-3. A pull-down assay of wild-type and polyQ-expanded GST-tagged ataxin-3 (GST-15Q and 77Q, respectively) revealed the binding of OGT to both ataxin-3 variants (Fig. 3*F*), hinting at a direct interaction between these two enzymes.

OGT Knockdown Reduces Soluble and Aggregated PolyQ-Expanded Ataxin-3. Overexpression of OGT and increased *O*-GlcNAcylation of key components for the autophagolysosome formation have been shown to suppress basal autophagy (20, 34). In cell and *Drosophila* models of HD (26) as well as in rat cortical neurons, mouse astrocytes (21, 35), and bladder cancer cells (36), strategies lowering OGT levels and activity improved clearance and attenuated protein toxicity. After observing increased OGT levels in our MJD models, we, likewise, aimed at targeting OGT as an attempt to improve the degradation of soluble and insoluble forms of polyQ-expanded ataxin-3. We first employed an endoribonuclease-prepared small interfering RNA (esiRNA)–-based strategy to lower OGT expression in 293T *ATXN3*$^{-/-}$ cells expressing wild-type (15Q) or polyQ-expanded (148Q) ataxin-3. Western blot analysis confirmed the reduction of OGT protein levels (Fig. 4*A*) and decreased global *O*-GlcNAcylation (Fig. 4*B*). Importantly, knockdown of OGT resulted in the reduction of soluble forms of both 15Q and 148Q ataxin-3 (Fig. 4*C*). Moreover, OGT knockdown decreased the amount of polyQ-expanded ataxin-3 aggregates, as shown by the immunodetection of ataxin-3 in the stacking gel (Fig. 4*C*), and of sodium dodecyl sulfate (SDS)-insoluble forms of ataxin-3, detected by filter retardation analysis of protein extracts (Fig. 4*D*). These results were further confirmed by fluorescence microscopy-based aggregate counting in cells expressing EGFP-tagged ataxin-3 148Q (Fig. 4*E*). Furthermore, OGT knockdown rescued the compromised cell viability of 293T *ATXN3*$^{-/-}$ cells expressing polyQ-expanded ataxin-3, as assessed via the resazurin-based PrestoBlue assay (Fig. 4*F*).

Our group reported that ataxin-3 is cleaved by calpains, which generates C-terminal, polyQ-containing fragments exhibiting increased aggregation propensity and cytotoxicity when compared to full-length ataxin-3 (37). As protein aggregation is a hallmark in MJD, we investigated whether OGT knockdown has comparable effects on a highly aggregation-prone, calpain-dependent fragment of ataxin-3 as on full-length ataxin-3. For this, wild-type 293T cells were cotransfected with EGFP-tagged, C-terminal ataxin-3 148Q fragment construct, representing a product of the calpain cleavage between amino acids D208 and L209 (EGFP-Atx3$_{209Cter}$ 148Q; *SI Appendix*, Fig. S3A), and esiRNAs targeting OGT. As for full-length ataxin-3, Western blot (*SI Appendix*, Fig. S3B) and filter retardation analyses (*SI Appendix*, Fig. S3C) of protein extracts revealed that OGT knockdown reduced soluble and aggregated forms of the highly aggregation-prone ataxin-3 cleavage product. Altogether, our observations suggest that a reduction of OGT has positive repercussions on the molecular pathogenesis of MJD by lowering toxic forms of mutant ataxin-3 and improving the compromised cell viability.

Pharmacological Inhibition of OGT Reduces PolyQ-Expanded Ataxin-3 Aggregates and Induces Autophagy. After successfully reducing soluble and aggregated forms of polyQ-expanded ataxin-3 via OGT knockdown, we intended to replicate this effect in a more translational practice by using OSMI-1, a specific pharmacological inhibitor of OGT activity (38). We established the optimal concentration of this compound in cell culture by assessing the impact of OSMI-1 on cell vitality and global *O*-GlcNAcylation levels. Assessment of cell morphology and growth (*SI Appendix*, Fig. S4A) as well as Western blot analysis of protein extracts from OSMI-1-treated wild-type 293T cells (*SI Appendix*, Fig. S4B) revealed a most-appropriate OSMI-1 concentration of 10 μM for this cell line. Next, we tested the effects of OSMI-1 treatment on soluble and aggregated forms of ataxin-3 in wild-type 293T cells transfected with ataxin-3 15Q or 148Q. Cells were supplied with OSMI-1-containing medium 24 h after transfection and incubated for further 24 h until lysis. Western blotting revealed a successful reduction of global *O*-GlcNAcylation in cells either expressing wild-type (15Q) or polyQ-expanded (148Q) ataxin-3 (*SI Appendix*, Fig. S4C). Analogous to OGT knockdown, OSMI-1 treatment reduced soluble mutant ataxin-3 (Fig. 5*A*). Moreover, filter retardation analysis of protein extracts also showed decreased aggregate levels of polyQ-expanded ataxin-3 upon OSMI-1 treatment (Fig. 5*B*), and OSMI-1-treated, patient-derived IHF presented a rescue in cell viability (Fig. 5*C*), altogether supporting OGT as a potential therapeutic target for MJD.

OGT is a regulator of the autophagic flux (20, 28), and ataxin-3 is a known autophagy substrate (39–41). After observing that both genetically lowering and pharmacological inhibition of OGT reduced soluble and aggregated forms of ataxin-3, we aimed at evaluating the impact of OSMI-1 treatment on autophagy stimulation. For this, 293T cells were treated with 10 μM OSMI-1 or vehicle (dimethyl sulfoxide [DMSO]) for 24 h, with a cotreatment of the autophagy inhibitor bafilomycin A1 (BafA1) for the last 4 h of culture. Protein extracts were analyzed via Western blotting to detect the autophagy markers p62 and LC3B-II, two proteins that are degraded by autophagy and accumulate upon BafA1 treatment, thereby serving as a measure of autophagic flux (42, 43). Although in the OSMI-1-treated condition there was no baseline difference for p62 and LC3B-II levels, under BafA1 incubation the OSMI-1-treated samples revealed a significant increase of both markers, suggesting elevated autophagic flux induced by pharmacological inhibition of OGT (Fig. 5*D*). Thus, the beneficial lowering of ataxin-3 levels by inhibiting OGT and, consequently, *O*-GlcNAcylation might be a result of enhanced autophagic flux, which

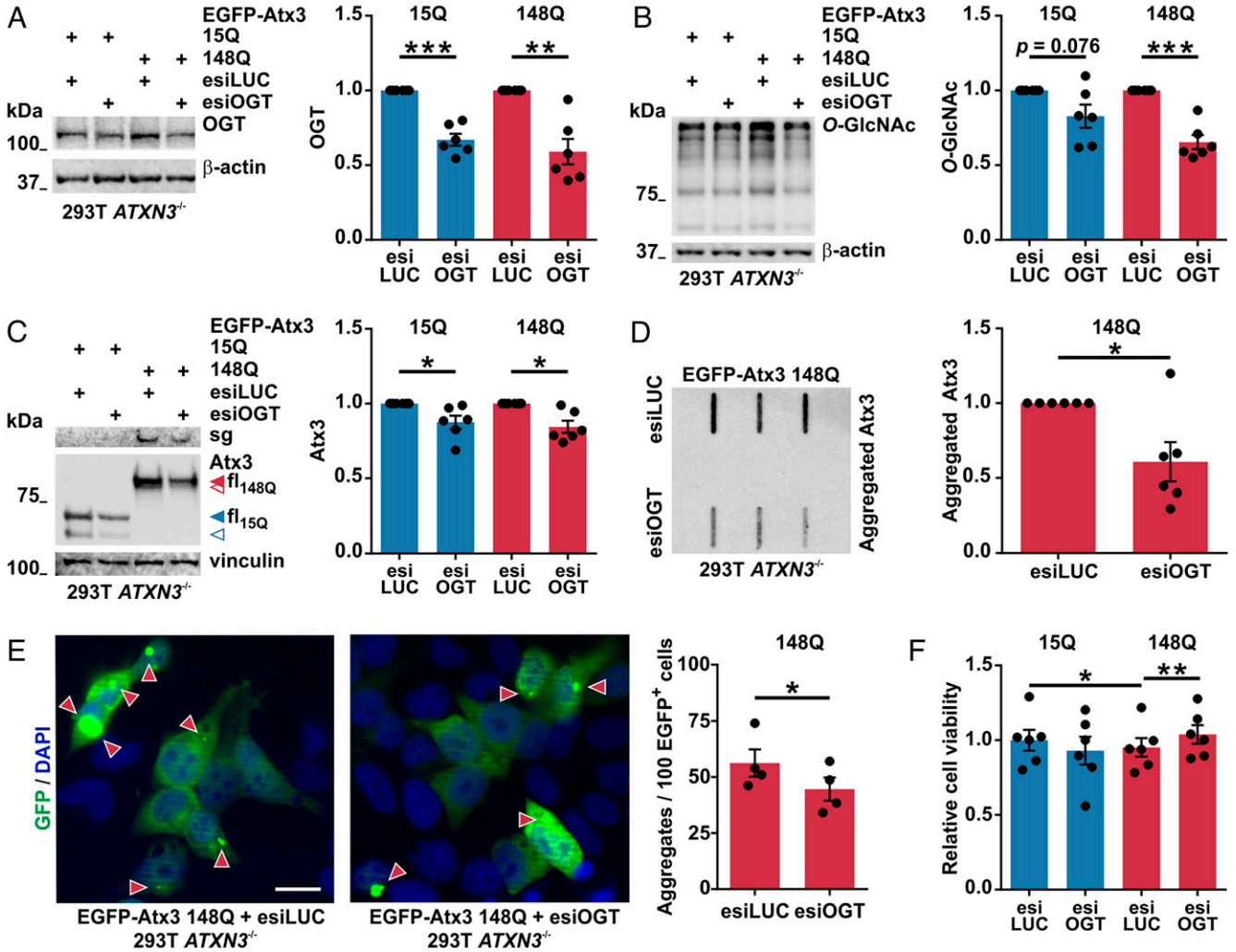

Fig. 4. OGT knockdown reduces soluble and aggregated forms of polyQ-expanded ataxin-3. (*A*) Western blot demonstrated OGT down-regulation by the OGT-targeting esiRNAs (esiOGT). 293T *ATXN3*$^{-/-}$ cells were transfected with EGFP-tagged wild-type (15Q) or polyQ-expanded (148Q) ataxin-3 and control (esiLUC) or esiOGT. β-actin served as loading control. $n = 6$ and one-sample *t* test; in 15Q esiLUC versus 15Q esiOGT, $P = 0.0004$; and in 148Q esiLUC versus 148Q esiOGT, $P = 0.005$. (*B*) Samples probed for *O*-GlcNAc confirmed the decreased *O*-GlcNAcylation upon OGT knockdown. $n = 6$ and one-sample *t* test; in 15Q esiLUC versus 15Q esiOGT, $P = 0.076$; and in 148Q esiLUC versus 148Q esiOGT, $P = 0.001$. (*C*) OGT knockdown reduced full-length (fl, blue and red arrowheads) and fragments (blue and red unfilled arrowheads) of both Atx3 15Q and 148Q, and reduced ataxin-3 148Q aggregates, as evidenced by the stacking gel (sg). Vinculin served as loading control. $n = 6$ and one-sample *t* test; in 15Q esiLUC versus 15Q esiOGT, $P = 0.037$; and in 148Q esiLUC versus 148Q esiOGT, $P = 0.012$. (*D*) Filter retardation analysis confirmed a decreased amount of Atx3 148Q aggregates upon OGT knockdown. $n = 6$, one-sample *t* test, and $P = 0.031$. (*E*) Fluorescence microscopy analysis also demonstrated a reduced number of aggregates (highlighted by arrowheads) under OGT knockdown (630× magnification). Scale bar, 20 μm. Data shows the percentage of aggregates in GFP-positive (EGFP^{+}) cells. $n = 4$, paired *t* test, and $P = 0.038$. (*F*) PrestoBlue assay of 293T *ATXN3*$^{-/-}$ cells transfected with Atx3 15Q or 148Q and esiLUC or esiOGT demonstrated an OGT knockdown-dependent rescue of the cell viability in cells expressing Atx3 148Q. Normalization was done to the mean of wild-type control group (15Q esiLUC). $n = 6$ and repeated measures one-way ANOVA with Tukey's post hoc test; in 15Q esiLUC versus 148Q esiLUC, $P = 0.033$; and in148Q esiLUC versus 148Q esiOGT, $P = 0.006$. Data are represented as means ± SEM $^{*}P \leq 0.05$, $^{**}P \leq 0.01$, and $^{***}P \leq 0.001$.

removes soluble and insoluble forms of the disease protein. Excessive *O*-GlcNAcylation is detrimental to neurons (28), and we observed beneficial consequences of OGT inhibition in transiently transfected and in patient-derived IHF cell models of MJD. For these reasons, we aimed at analyzing the repercussion of OGT inhibition in MJD iCN using different concentrations of OSMI-1 as well as different treatment duration. We treated iCN from three MJD patients with 10 μM OSMI-1 for 24 h or 72 h, and 30 μM OSMI-1 for 24 h. Microscopy analysis of cell morphology confirmed that the drug was well tolerated by the iCN at all concentrations and treatment times tested (*SI Appendix*, Fig. S4D). Western blot analysis demonstrated an increase of LC3B-II in all treatment conditions (*SI Appendix*, Fig. S4E), further suggesting an induction of autophagy in the MJD iCN. All OSMI-1 treatment conditions led to a reduction of polyQ-expanded ataxin-3-soluble levels (Fig. 5*E*, Atx3 fl_{exp}), although administration of 30 μM OSMI-1 for 24 h was the most effective. Strikingly, OSMI-1 treatment at 10 μM for 24 h resulted in the reduction of polyQ-expanded ataxin-3 levels without significantly altering wild-type ataxin-3 in transfected cells (Fig. 5*A*) and in MJD iCN (Fig. 5*E*, Atx3 fl_{wt}). Importantly, all OSMI-1 treatment approaches also culminated in reduced polyQ-expanded ataxin-3 aggregates, as assessed via filter retardation analysis of SDS-insoluble ataxin-3 (Fig. 5*F*).

Pharmacological Inhibition of OGT Alleviates Motor Impairment of MJD Zebrafish. After observing an attenuation of the molecular pathology upon OSMI-1 treatment in transiently transfected

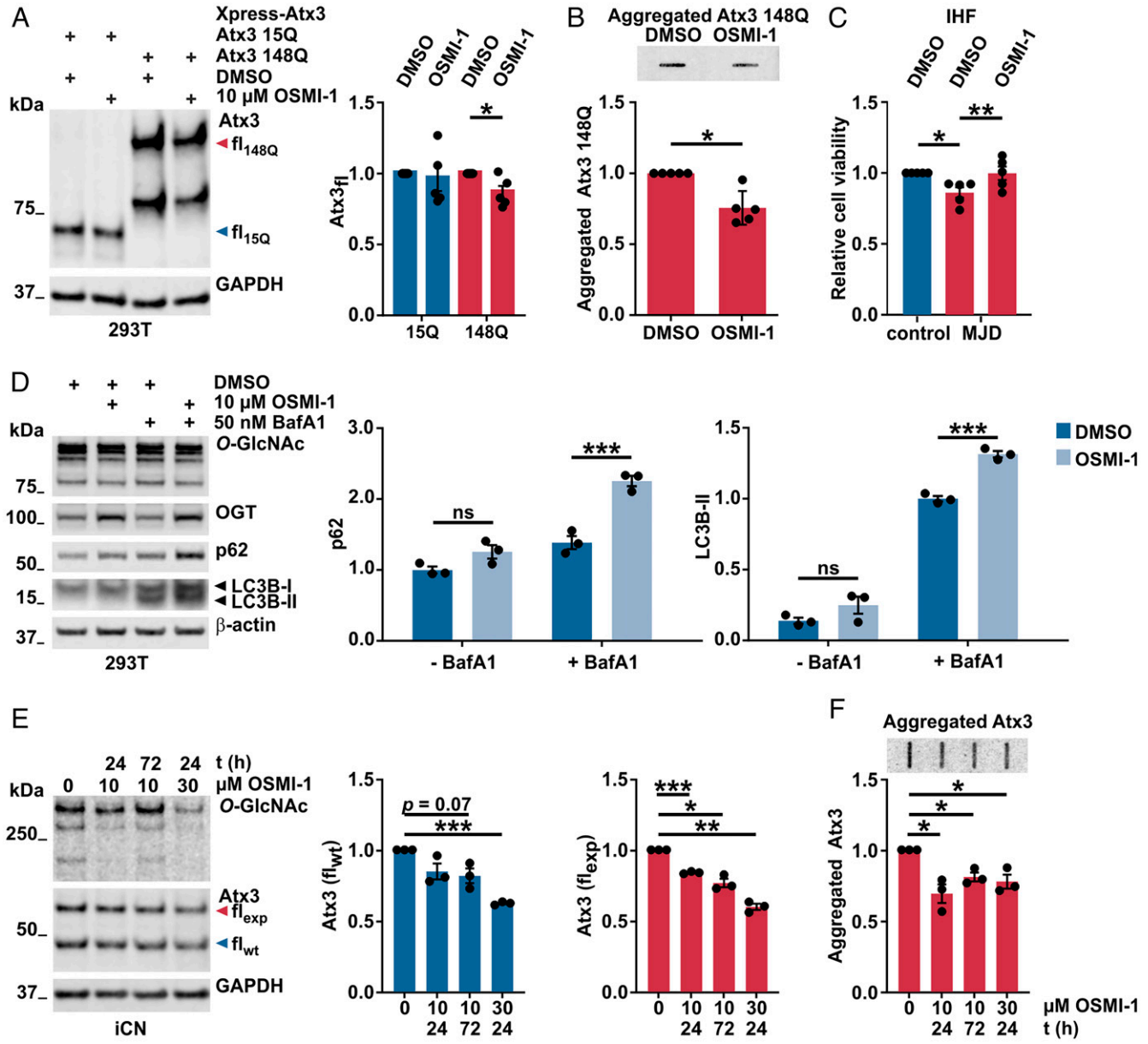

Fig. 5. Pharmacological inhibition of OGT reduces polyQ-expanded ataxin-3 levels and aggregates and increases autophagy. (*A*) Western blot analysis of protein extracts revealing that full-length Atx3 148Q (fl148Q, red arrowhead) was reduced upon OGT inhibition, while Atx3 15Q (fl15Q, blue arrowhead) remained unchanged. GAPDH served as loading control. $n = 5$ and one-sample t test; in 148Q DMSO versus 148Q OSMI-1, $P = 0.044$. (*B*) Filter retardation analysis of samples used in *A*, showing decreased aggregation of Atx3 148Q upon OSMI-1 treatment. $n = 5$, one-sample t test, and $P = 0.010$. (*C*) Cell-viability analysis of IHF derived from one control and one MJD patient demonstrating impaired viability of the MJD line, which was rescued by a 24 h treatment with 10 μM OSMI-1. $n = 5$, control DMSO versus control MJD, one-sample t test, and $P = 0.021$; in MJD DMSO versus MJD OSMI-1, paired t test and $P = 0.0023$. (*D*) Western blot for analysis of autophagy markers LC3B-II and p62 in 293T samples obtained after 10 μM OSMI-1 treatment plus 50 nM of the autophagy inhibitor BafA1 4 h before harvesting. Elevated LC3B-II and p62 levels upon OSMI-1 and BafA1 treatment suggest increased autophagic flux. β-actin served as loading control. - BafA1 = without BafA1; and + BafA1 = with BafA1. $n = 3$ and two-way ANOVA with Sidak's post hoc test; in 10 μM OSMI-1 BafA1 versus DMSO BafA1, $P = 0.0001$ for p62 and $P = 0.001$ for LC3-II. (*E*) Western blot of iCN from MJD patients showing the reduction of global *O*-GlcNAc and of soluble ataxin-3 in samples treated with OSMI-1. Treatment of iCN derived from three MJD patients with 10 μM OSMI-1 for 24 h or 72 h, or 30 μM OSMI-1 for 24 h resulted in decreased polyQ-expanded ataxin-3 (Atx3 fl_{exp}, red arrowhead) in all three conditions compared to DMSO control (0 μM OSMI-1), whereas a significant reduction of WT Atx3 (Atx3 fl_{wt}, blue arrowhead) was only achieved with 30 μM OSMI-1 for 24 h GAPDH served as loading control. $n = 3$ and one-sample t test; in Atx3 fl_{wt}. 0 versus 30 μM OSMI-1, $P = 0.0003$; in Atx3 fl_{exp} 0 versus 10 μM OSMI-1 24 h, $P = 0.0008$; in Atx3 fl_{exp} 0 versus 10 μM OSMI-1 72 h, $P = 0.016$; and in Atx3 fl_{exp} 0 versus 30 μM OSMI-1 24 h, $P = 0.003$. (*F*) Filter retardation analysis of samples used in *E* revealing a reduction of ataxin-3 protein aggregates upon OSMI-1 treatment. $n = 3$ and one-sample t test; in 0 versus 10 μM OSMI-1 24 h, $P = 0.043$; in 0 versus 10 μM OSMI-1 72 h, $P = 0.026$; and in 0 versus 30 μM OSMI-1, $P = 0.046$. Data are represented as means ± SEM $*P \leq 0.05$, $**P \leq 0.01$, $***P \leq 0.001$, and ns = not significant.

and in patient-derived MJD cell models, we aimed at reproducing the beneficial effects of OGT inhibition in vivo. For this purpose, we made use of an established transgenic zebrafish model (44) of MJD. Western blot analysis of protein extracts from zebrafish larvae neuronally expressing EGFP-tagged, non-expanded (23Q) or polyQ-expanded (84Q) human ataxin-3 revealed that, in line with our data in cell and mouse models, OGT protein levels are increased in ataxin-3 84Q zebrafish,

compared to fish expressing ataxin-3 23Q (Fig. 6*A*). Therefore, we proceeded to the pharmacological inhibition of OGT via OSMI-1 treatment. The treatment was performed between 1 and 6 d post fertilization at two different concentrations of OSMI-1, 8 μM and 16 μM. Unexpectedly, Western blot analysis revealed a significant reduction of OGT at 16 μM OSMI-1 treatment (Fig. 6*B*). Ataxin-3 full-length and cleavage products were also strongly reduced at 16 μM OSMI-1 treatment (Fig. 6*C*), which might explain the observed decrease of OGT, since we also recognized lower OGT levels in cells lacking ataxin-3 (Fig. 2 *A* and *C*). As described previously (44), zebrafish larvae expressing polyQ-expanded ataxin-3 (84Q) swam shorter distances in periods of darkness compared to those expressing a shorter polyQ repeat (23Q) (Fig. 6*D*). OSMI-1 treatment at both 8 μM and 16 μM resulted in an increase of the total swimming distance compared to the vehicle (DMSO)-treated ataxin-3 84Q animals (Fig. 6*D*), although not to the extent of the ataxin-3 23Q zebrafish (Fig. 6*D*). To analyze the impact of OSMI-1 treatment in histological hallmarks of MJD, we performed confocal microscopy of the zebrafish expressing ataxin-3 84Q. Imaging of the spinal cord revealed the presence of ataxin-3 aggregates, which was reduced in the zebrafish treated with 16 μM OSMI-1 (Fig. 6*E*). To quantify this reduction on ataxin-3 aggregates, dissociated cells of the 84Q zebrafish were analyzed via flow cytometry, as described previously (45). Flow cytometric analysis confirmed a 30% reduction of ataxin-3 aggregates in the 84Q zebrafish treated with 16 μM OSMI-1 (Fig. 6*F*).

Collectively, the in vivo data obtained from the MJD zebrafish treatment validated our cell culture–based findings on the benefits of pharmacological inhibition of OGT in the context of the MJD molecular pathology, further demonstrating profitable effects on the impaired motor function, a hallmark in MJD.

Discussion

The discovery of *O*-GlcNAcylation as a relevant PTM in the molecular pathogenesis of neurodegenerative disorders highlights this pathway as a promising target for those yet incurable conditions (27, 46). However, knowledge in the field is still scarce, and some available conclusions seem conflicting. In our study, we demonstrated that first, transiently transfected and patient-derived MJD cells as well as MJD mouse and zebrafish models present a dysregulation of the vitally important OGT enzyme; second, ataxin-3 modulates OGT protein levels and ubiquitination status, presumably preventing its proteasomal degradation; and third, lowering OGT levels or activity reduces soluble and insoluble species of polyQ-expanded ataxin-3 in cellulo and in vivo, and alleviates the motor impairment in an MJD zebrafish model.

O-GlcNAcylation levels often correlate with the amount of OGT, the sole enzyme catalyzing this PTM (47, 48), and our results obtained from three MJD cell models, MJD transgenic mice, and MJD zebrafish demonstrated increased levels of this enzyme. Accordingly, we observed elevated global *O*-GlcNAcylation levels in transfected 293T *ATXN3*$^{-/-}$ cells and SV40-immortalized fibroblasts expressing polyQ-expanded ataxin-3, portraying in MJD what has been recently reported in postmortem brain of PD patients (28).

In contrast, baseline *O*-GlcNAcylation levels were reportedly decreased in AD patient brain (49). Increasing *O*-GlcNAcylation slowed neurodegeneration and reduced levels of amyloid plaques or phosphorylation-mediated tau oligomerization (50–53). However, another study of AD patient brain revealed increased *O*-GlcNAcylation and decreased OGA levels (54). Additional data from an AD mouse model showed that OGA inhibition increases *O*-GlcNAcylation in a single motif within tau, without altering its global phosphorylation (55). Findings in HD are as divergent, since pharmacological inhibition of OGA avoided disruption of the nuclear pore complex by mutant huntingtin (7), but inhibition of *O*-GlcNAcylation in HD cells or flies alleviated the disease phenotype (26), which is in line with our data on reduction of *O*-GlcNAcylation via genetically and pharmacologically targeting OGT in MJD.

We further analyzed the influence of ataxin-3 on OGT levels and demonstrated that the lack of ataxin-3 in cell and animal models led to reduced OGT. In addition, OGT presented lower stability in 293T *ATXN3*$^{-/-}$ cells, and the expression of wild-type ataxin-3 rescued OGT protein levels without altering its mRNA levels.

OGT is deubiquitinated and stabilized by the DUB BAP1 (56), and as a DUB (13), ataxin-3 could have a similar activity. Indeed, in our experiments, 293T *ATXN3*$^{-/-}$ cells presented a stronger accumulation of high–molecular weight OGT bands compared to wild-type cells, suggesting an increased amount of ubiquitinated OGT in the absence of ataxin-3. When 293T *ATXN3*$^{-/-}$ or IHF lysates were incubated with purified ataxin-3, OGT immunoblot revealed a time-dependent reduction of those high–molecular weight bands, implying an enzyme–substrate interaction between ataxin-3 and OGT. Interestingly, in our DUB assays, ataxin-3 preferentially processed K48-linked over K63-linked Ub chains, contrasting with a study on ataxin-3's DUB activity (57). Typically, K48-linked Ub chains are associated to protein degradation via the UPS, whereas K63-linked Ub chains were demonstrated to selectively target protein aggregates to autophagic degradation (58, 59). Therefore, our finding suggests a more-relevant role of ataxin-3's DUB activity for the outcome of proteins degraded via the UPS, as proposed previously (60).

Immunoprecipitation of ubiquitinated proteins revealed a high–molecular weight OGT band, which appeared weaker in cells expressing polyQ-expanded ataxin-3 when compared to cells expressing wild-type ataxin-3, proposing a greater DUB activity of polyQ-expanded ataxin-3 toward OGT. This result is in line with the reduced Ub OGT levels observed in MJD IHF at baseline and with previous studies demonstrating that polyQ-expanded ataxin-3 deubiquitinates its substrates parkin and p53 with higher efficiency than wild-type ataxin-3 (31, 33). Finally, our GST pull-down assays revealed that both wild-type and mutant ataxin-3 might directly interact with OGT. Therefore, ataxin-3 presumably controls OGT protein clearance via regulating its ubiquitination.

Since we found that *O*-GlcNAcylation is dysregulated in MJD models, we tested whether an intervention on this pathway could alleviate the molecular pathogenesis caused by polyQ-expanded ataxin-3. OGT knockdown or its pharmacological inhibition resulted in decreased levels of soluble and aggregated ataxin-3 in MJD cell models. Moreover, both approaches rescued the viability of cells expressing polyQ-expanded ataxin-3. Similar results were observed in a *C. elegans* model for HD bearing a null mutation in the OGT gene homolog *ogt-1*, which presented amelioration of the phenotype, absence of polyQ toxicity-associated animal death, and reduced number of N-terminal huntingtin aggregates (11). Notably, pharmacological inhibition of OGT in MJD zebrafish, which features an impaired swimming phenotype mimicking the progressive cerebellar ataxia of MJD patients (61), reduced polyQ-expanded ataxin-3 levels and improved its motor impairment. This finding corroborates our hypothesis that OGT may constitute a promising target for treating MJD.

How could the lowering of OGT levels or activity ameliorate the molecular pathogenesis in MJD? OGT is known to regulate autophagy via *O*-GlcNAcylation of multiple key components. On one hand, OGT promotes *O*-GlcNAcylation and activation of Unc-51-like kinase 1 (ULK1) (62), which is required for phagophore formation and initiation of autophagy (63). On the

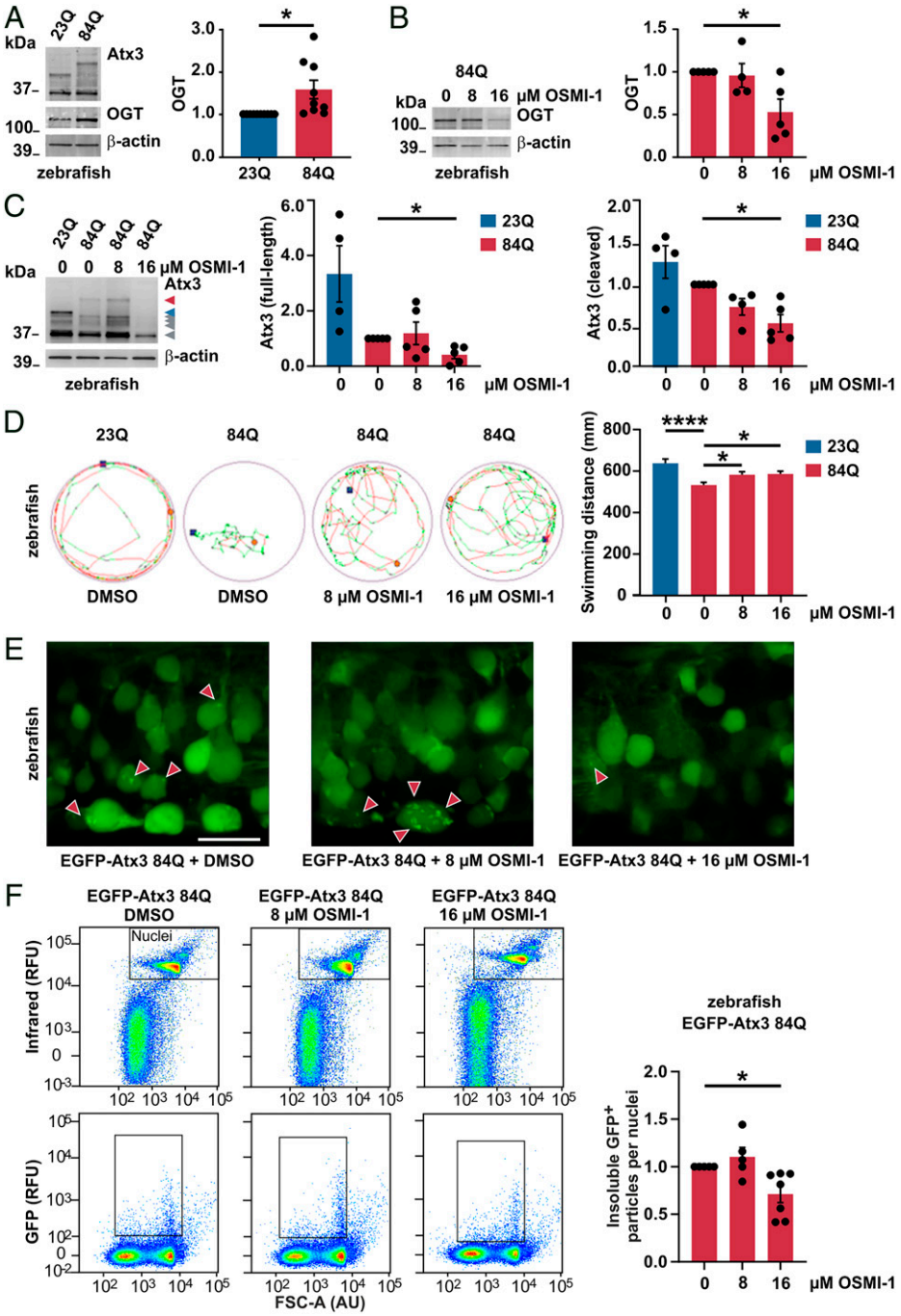

Fig. 6. Counteracting increased OGT via its pharmacological inhibition reduces polyQ-expanded ataxin-3 levels and aggregates, alleviating motor phenotype in MJD zebrafish model. (*A*) Western blot of samples from MJD zebrafish larvae (84Q) and its wild-type control (23Q), depicting a baseline increase of OGT in the ataxin-3 84Q fish. β-actin served as loading control. $n = 9$ to 10, one-sample t test, and $P = 0.028$. (*B*) Western blot demonstrating the reduction of OGT upon 16 μM OSMI-1 treatment of Atx3 84Q zebrafish. β-actin served as loading control. $n = 5$ and one-sample t test; in 0 versus 16 μM OSMI-1, $P = 0.036$. (*C*) Treatment of Atx3 84Q zebrafish with 16 μM OSMI-1 also reduced Atx3 full-length (red arrowhead) and cleavage products (gray arrowheads), as demonstrated on Western blot. β-actin served as loading control. $n = 4$ to 5, one-sample t test; in Atx3 full-length 0 versus 16 μM OSMI-1, $P = 0.014$; and in Atx3 cleaved 0 versus 16 μM OSMI-1, $P = 0.011$. (*D*) Representative images of the total distance swum on a tracking system by the Atx3 23Q and 84Q DMSO-treated transgenic zebrafish and the Atx3 84Q OSMI-1-treated fish at the concentrations of 8 μM and 16 μM. Images revealed a baseline impaired swimming pattern for the 84Q fish (DMSO) when compared to the 23Q fish and an improvement of the motor function in the 84Q OSMI-1-treated fish. The graph displays the quantification of the total swum distance of the transgenic zebrafish in all conditions depicted in the images. $n = 184$ (23Q), 247 (84Q 0 μM), 210 (84Q 8 μM), 246 (84Q 16 μM); one-way ANOVA with Dunett's post hoc test; in 23Q versus 84Q DMSO (0 μM OSMI-1), $P < 0.0001$; in 84Q 0 versus 8 μM OSMI-1, $P = 0.049$; and in 84Q 0 versus 16 μM, $P = 0.022$. (*E*) Confocal imaging of the Atx3 84Q zebrafish spinal cord demonstrating the reduction of ataxin-3 aggregates (red arrowheads) upon OSMI-1 treatment at 16 μM (400× magnification). Scale bar, 15 μm. (*F*) Flow cytometric analysis of dissociated zebrafish cells expressing EGFP-tagged Atx3 84Q demonstrated the reduction of ataxin-3 aggregates (insoluble GFP^+ particles) upon 16 μM OSMI-1 treatment. Nuclei of live cells were stained and identified based on the intensity of infrared fluorescence. RFU, relative fluorescence units; FSC-A (AU), forward scatter area, arbitrary unit. The graph displays the quantification of ataxin-3 aggregates at 0 μM (DMSO), 8 μM, and 16 μM OSMI-1 treatment. $n = 5$ to 7, one-sample t test, and $P = 0.018$. Data are represented as means ± SEM, $^*P \leq 0.05$, and $^{****}P \leq 0.0001$.

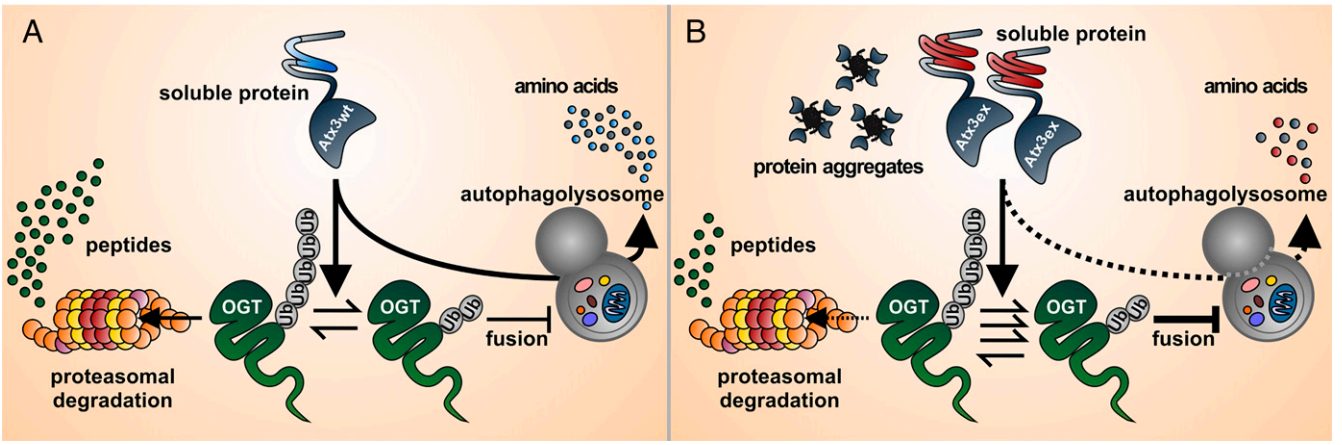

Fig. 7. Schematic representation of the proposed interplay between ataxin-3 and OGT in protein clearance. (*A*) Under physiological conditions, wild-type ataxin-3 (Atx3wt) serves as a DUB to OGT, partly rescuing the latter from proteasomal degradation and thereby indirectly lowering autophagic flux (20). This counteracts the positive autophagy regulation by ataxin-3 (64). The equilibrium between positive and negative feedback of wild-type ataxin-3 toward autophagy allows a proper degradation of misfolded proteins and compromised organelles in a healthy cellular context. (*B*) In MJD, polyQ-expanded ataxin-3 (Atx3ex) presents enhanced DUB activity toward OGT, which culminates in reduced degradation and thus increased OGT protein levels. This process leads to a further suppression and impairment of autophagy by preventing autophagosome–lysosome fusion (20), ultimately resulting in accumulation of toxic soluble and aggregated forms of polyQ-expanded ataxin-3.

other hand, reduction of *O*-GlcNAcylation enables an increase of the autophagosome–lysosome fusion, therefore boosting the autophagic flux (20). Furthermore, overexpression of OGT was shown to reduce expression of autophagy genes and the number of autophagosomes (34). Indeed, our experiments on pharmacological inhibition of OGT via administration of OSMI-1 in wild-type 293T cells and in patient-derived iCN pointed to an induction of the autophagic flux. Thus, the increased OGT levels observed in our various cell and animal models may contribute to the known autophagic impairment in MJD (22, 23), which has been primarily associated with a dysregulation of the autophagy-initiating factor beclin-1 (64).

Based on our findings and previous reports, we propose a mutual modulation between OGT and ataxin-3 in protein clearance control, with consequences for the molecular pathogenesis in MJD (Fig. 7). While the physiological DUB activity of ataxin-3 is important for driving early stages of autophagy (64), the DUB activity of polyQ-expanded ataxin-3 might have detrimental consequences in the final stages of the autophagic process, when leading to accumulation of OGT and triggering inhibitory *O*-GlcNAcylation of key components of the autophagosome-lysosome fusion (20). This consideration is supported by previous observations of increased DUB activity of polyQ-expanded ataxin-3 (30, 32).

Conclusion

Our results endorse the importance of OGT and the *O*-GlcNAc cycle in polyQ-related neurodegenerative disorders by revealing their pathological alteration in MJD. We show that ataxin-3 has a physiological role in regulating OGT protein levels and its ubiquitination status. We propose that by downregulating *O*-GlcNAcylation via OGT lowering or pharmacological inhibition, we likely up-regulate protein clearance via autophagy and thereby reduce toxic species of the MJD protein ataxin-3. Hence, we believe that OGT constitutes an auspicious candidate for the development of therapeutics for MJD and perhaps also for other yet incurable neurodegenerative disorders.

Materials and Methods

Please refer to *SI Appendix* for a detailed description of the materials and methods.

Ethical Statement. Mouse experiments were approved based on European Union legislation (Directive 2010/63/EU). Generation of cell lines from fibroblasts was approved by the ethics committee of the University of Tübingen (598/2011BO1). Zebrafish experiments were conducted in accordance with the animal ethics committee of Macquarie University (ARA: 2016/004).

Animals and Tissue Sampling. Mice were kept as previously described (30, 65) and euthanized by CO_2 inhalation.

Larvae from MJD transgenic zebrafish (44) were used for treatment, behavior analysis, and lysate preparation.

Treatment and Behavioral Analysis of MJD Zebrafish. Embryos were treated with OSMI-1 (Cayman Chemical) or DMSO until 6 d postfertilization. Motor function was assessed using the Zebrabox tracking system (Viewpoint).

Cell Culture and Transfection. Fibroblasts were reprogrammed and differentiated as described previously (66, 67). Please refer to *SI Appendix* for a full description of the cell lines, constructs, and transfection reagents used.

Cell-Viability Assay. Cell viability was assessed using PrestoBlue assay (Thermo Fisher Scientific).

In Vitro Deubiquitination Assay. 293T *ATXN3*$^{-/-}$ and IHF lysates were incubated with 0.25 μM of human His_6-ataxin-3 (E-341, BioTechne GmbH) for up to 2 h. Reactions were terminated in 4× lithium dodecyl sulfate (LDS) sample buffer and 100 mM dithiothreitol.

Cell-Based Treatments. Cells were treated with the compounds OSMI-1, Thiamet G, CHX, MG132 (all Sigma-Aldrich), or BafA1 (Invivogen).

Fluorescence Microscopy, Confocal Microscopy of MJD Zebrafish, GFP Immunoprecipitation, and GST Pull-down. Please refer to *SI Appendix* for a full description of these methods.

Protein Extraction, Western Blotting, and Filter Retardation Assay. Extracts were prepared in supplemented radioimmunoprecipitation assay (RIPA) buffer. Western blotting and filter retardation assay were performed as described previously (37).

Flow Cytometric Analysis of Detergent-Insoluble Protein Species. The total number of detergent-insoluble EGFP+ particles in the EGFP-tagged ataxin-3 84Q zebrafish was analyzed relative to the total number of nuclei and calculated for each sample of dissociated cells.

Real-Time qPCR. Relative expression levels were calculated based on Pfaffl model (68). Please refer to *SI Appendix* for a full description of this method.

Statistical Analysis. Statistical significance was determined using two-tailed Student's *t* test and one-way or two-way ANOVA, with the respective posttests.

Data Availability. All study data are included in the article and/or *SI Appendix*.

ACKNOWLEDGMENTS. We thank Prof. Nico Dantuma (Karolinska Institutet, Solna, Sweden) for providing the GFP-Ub construct. The work was supported by the German Ministry of Education and Research (EU Joint Programme - Neurodegenerative Disease Research - JPND Grant 01ED1602B to L.S.). The zebrafish work was supported by the Machado Joseph Disease Foundation within Australia (grant to A.S.L). P.P.S. thanks the Brazilian National Council for Scientific and Technological Development and the German Academic Exchange Service for the financial support within the "Science without Borders" program (Process 229957/2013-7). L.S. and O.R. are members of the European Reference Network for Rare Neurological Diseases (Project 739510).

1. I. Akan, S. Olivier-Van Stichelen, M. R. Bond, J. A. Hanover, Nutrient-driven O-GlcNAc in proteostasis and neurodegeneration. *J. Neurochem.* **144**, 7–34 (2018).
2. C. R. Torres, G. W. Hart, Topography and polypeptide distribution of terminal N-acetylglucosamine residues on the surfaces of intact lymphocytes. Evidence for O-linked GlcNAc. *J. Biol. Chem.* **259**, 3308–3317 (1984).
3. L. K. Kreppel, M. A. Blomberg, G. W. Hart, Dynamic glycosylation of nuclear and cytosolic proteins. Cloning and characterization of a unique O-GlcNAc transferase with multiple tetratricopeptide repeats. *J. Biol. Chem.* **272**, 9308–9315 (1997).
4. Y. Gao, L. Wells, F. I. Comer, G. J. Parker, G. W. Hart, Dynamic O-glycosylation of nuclear and cytosolic proteins: Cloning and characterization of a neutral, cytosolic beta-N-acetylglucosaminidase from human brain. *J. Biol. Chem.* **276**, 9838–9845 (2001).
5. F. Liu, K. Iqbal, I. Grundke-Iqbal, G. W. Hart, C.-X. Gong, O-GlcNAcylation regulates phosphorylation of tau: A mechanism involved in Alzheimer's disease. *Proc. Natl. Acad. Sci. U.S.A.* **101**, 10804–10809 (2004).
6. N. P. Marotta *et al.*, O-GlcNAc modification blocks the aggregation and toxicity of the protein α-synuclein associated with Parkinson's disease. *Nat. Chem.* **7**, 913–920 (2015).
7. J. C. Grima *et al.*, Mutant huntingtin disrupts the nuclear pore complex. *Neuron* **94**, 93–107.e6 (2017).
8. G. W. Hart, M. P. Housley, C. Slawson, Cycling of O-linked beta-N-acetylglucosamine on nucleocytoplasmic proteins. *Nature* **446**, 1017–1022 (2007).
9. P. März *et al.*, Ataxin-10 interacts with O-linked beta-N-acetylglucosamine transferase in the brain. *J. Biol. Chem.* **281**, 20263–20270 (2006).
10. P. Wang, J. A. Hanover, Nutrient-driven O-GlcNAc cycling influences autophagic flux and neurodegenerative proteotoxicity. *Autophagy* **9**, 604–606 (2013).
11. P. Wang *et al.*, O-GlcNAc cycling mutants modulate proteotoxicity in *Caenorhabditis elegans* models of human neurodegenerative diseases. *Proc. Natl. Acad. Sci. U.S.A.* **109**, 17669–17674 (2012).
12. B. P. C. van de Warrenburg *et al.*, Spinocerebellar ataxias in the Netherlands: Prevalence and age at onset variance analysis. *Neurology* **58**, 702–708 (2002).
13. B. Burnett, F. Li, R. N. Pittman, The polyglutamine neurodegenerative protein ataxin-3 binds polyubiquitylated proteins and has ubiquitin protease activity. *Hum. Mol. Genet.* **12**, 3195–3205 (2003).
14. T. Schmidt *et al.*, An isoform of ataxin-3 accumulates in the nucleus of neuronal cells in affected brain regions of SCA3 patients. *Brain Pathol.* **8**, 669–679 (1998).
15. C. A. Matos, S. de Macedo-Ribeiro, A. L. Carvalho, Polyglutamine diseases: The special case of ataxin-3 and Machado-Joseph disease. *Prog. Neurobiol.* **95**, 26–48 (2011).
16. P.-S. Wang, R.-S. Liu, B.-H. Yang, B.-W. Soong, Regional patterns of cerebral glucose metabolism in spinocerebellar ataxia type 2, 3 and 6: A voxel-based FDG-positron emission tomography analysis. *J. Neurol.* **254**, 838–845 (2007).
17. J. A. M. Saute *et al.*, Serum insulin-like system alterations in patients with spinocerebellar ataxia type 3. *Mov. Disord.* **26**, 731–735 (2011).
18. J. Cunha-Santos *et al.*, Caloric restriction blocks neuropathology and motor deficits in Machado-Joseph disease mouse models through SIRT1 pathway. *Nat. Commun.* **7**, 11445 (2016).
19. C. Han *et al.*, O-GlcNAcylation of SIRT1 enhances its deacetylase activity and promotes cytoprotection under stress. *Nat. Commun.* **8**, 1491 (2017).
20. B. Guo *et al.*, O-GlcNAc-modification of SNAP-29 regulates autophagosome maturation. *Nat. Cell Biol.* **16**, 1215–1226 (2014).
21. M. A. Rahman, Y. Cho, H. Hwang, H. Rhim, Pharmacological inhibition of O-GlcNAc transferase promotes mTOR-dependent autophagy in rat cortical neurons. *Brain Sci.* **10**, 1–17 (2020).
22. I. Onofre *et al.*, Fibroblasts of Machado Joseph disease patients reveal autophagy impairment. *Sci. Rep.* **6**, 28220 (2016).
23. A. Sittler *et al.*, Deregulation of autophagy in postmortem brains of Machado-Joseph disease patients. *Neuropathology* **38**, 113–124 (2018).
24. R. A. Nixon, The role of autophagy in neurodegenerative disease. *Nat. Med.* **19**, 983–997 (2013).
25. J. J. Weber, P. Pereira Sena, E. Singer, H. P. Nguyen, Killing two angry birds with one stone: Autophagy activation by inhibiting calpains in neurodegenerative diseases and beyond. *BioMed Res. Int.* **2019**, 4741252 (2019).
26. A. Kumar *et al.*, Decreased O-linked GlcNAcylation protects from cytotoxicity mediated by huntingtin exon1 protein fragment. *J. Biol. Chem.* **289**, 13543–13553 (2014).
27. W. Y. Wani, J. C. Chatham, V. Darley-Usmar, L. L. McMahon, J. Zhang, O-GlcNAcylation and neurodegeneration. *Brain Res. Bull.* **133**, 80–87 (2017).
28. W. Y. Wani *et al.*, O-GlcNAc regulation of autophagy and α-synuclein homeostasis; implications for Parkinson's disease. *Mol. Brain* **10**, 32 (2017).
29. Y. Yang, X. Yin, H. Yang, Y. Xu, Histone demethylase LSD2 acts as an E3 ubiquitin ligase and inhibits cancer cell growth through promoting proteasomal degradation of OGT. *Mol. Cell* **58**, 47–59 (2015).
30. I. Schmitt *et al.*, Inactivation of the mouse Atxn3 (ataxin-3) gene increases protein ubiquitination. *Biochem. Biophys. Res. Commun.* **362**, 734–739 (2007).
31. H. Liu *et al.*, The Machado-Joseph disease deubiquitinase ataxin-3 regulates the stability and apoptotic function of p53. *PLoS Biol.* **14**, e2000733 (2016).
32. N. P. Dantuma, T. A. M. Groothuis, F. A. Salomons, J. Neefjes, A dynamic ubiquitin equilibrium couples proteasomal activity to chromatin remodeling. *J. Cell Biol.* **173**, 19–26 (2006).
33. T. M. Durcan *et al.*, The Machado-Joseph disease-associated mutant form of ataxin-3 regulates parkin ubiquitination and stability. *Hum. Mol. Genet.* **20**, 141–154 (2011).
34. S. Park *et al.*, O-GlcNAc modification is essential for the regulation of autophagy in *Drosophila* melanogaster. *Cell. Mol. Life Sci.* **72**, 3173–3183 (2015).
35. M. A. Rahman, H. Hwang, Y. Cho, H. Rhim, Modulation of O-GlcNAcylation regulates autophagy in cortical astrocytes. *Oxid. Med. Cell. Longev.* **2019**, 6279313 (2019).
36. L. Jin *et al.*, Blockage of O-linked GlcNAcylation induces AMPK-dependent autophagy in bladder cancer cells. *Cell. Mol. Biol. Lett.* **25**, 17 (2020).
37. J. J. Weber *et al.*, A combinatorial approach to identify calpain cleavage sites in the Machado-Joseph disease protein ataxin-3. *Brain* **140**, 1280–1299 (2017).
38. R. F. Ortiz-Meoz *et al.*, A small molecule that inhibits OGT activity in cells. *ACS Chem. Biol.* **10**, 1392–1397 (2015).
39. F. M. Menzies *et al.*, Autophagy induction reduces mutant ataxin-3 levels and toxicity in a mouse model of spinocerebellar ataxia type 3. *Brain* **133**, 93–104 (2010).
40. Z. Ou *et al.*, Autophagy promoted the degradation of mutant ATXN3 in neurally differentiated spinocerebellar ataxia-3 human induced pluripotent stem cells. *BioMed Res. Int.* **2016**, 6701793 (2016).
41. D. Weishäupl *et al.*, Physiological and pathophysiological characteristics of ataxin-3 isoforms. *J. Biol. Chem.* **294**, 644–661 (2019).
42. R. A. Gottlieb, A. M. Andres, J. Sin, D. P. J. Taylor, Untangling autophagy measurements: All fluxed up. *Circ. Res.* **116**, 504–514 (2015).
43. S. R. Yoshii, N. Mizushima, Monitoring and measuring autophagy. *Int. J. Mol. Sci.* **18**, 1865 (2017).
44. M. Watchon *et al.*, Calpain inhibition is protective in Machado-Joseph disease zebrafish due to induction of autophagy. *J. Neurosci.* **37**, 7782–7794 (2017).
45. K. J. Robinson *et al.*, Flow cytometry allows rapid detection of protein aggregates in cellular and zebrafish models of spinocerebellar ataxia 3. *Dis. Model. Mech.* **14**, dmm049023 (2021).
46. S. A. Ansari, B. S. Emerald, The role of insulin resistance and protein O-GlcNAcylation in neurodegeneration. *Front. Neurosci.* **13**, 473 (2019).
47. C. L. Dai, J. H. Gu, F. Liu, K. Iqbal, C.-X. Gong, Neuronal O-GlcNAc transferase regulates appetite, body weight, and peripheral insulin resistance. *Neurobiol. Aging* **70**, 40–50 (2018).
48. H. M. Itkonen *et al.*, High OGT activity is essential for MYC-driven proliferation of prostate cancer cells. *Theranostics* **9**, 2183–2197 (2019).
49. F. Liu *et al.*, Reduced O-GlcNAcylation links lower brain glucose metabolism and tau pathology in Alzheimer's disease. *Brain* **132**, 1820–1832 (2009).
50. N. B. Hastings *et al.*, Inhibition of O-GlcNAcase leads to elevation of O-GlcNAc tau and reduction of tauopathy and cerebrospinal fluid tau in rTg4510 mice. *Mol. Neurodegener.* **12**, 39 (2017).
51. S. A. Yuzwa *et al.*, A potent mechanism-inspired O-GlcNAcase inhibitor that blocks phosphorylation of tau in vivo. *Nat. Chem. Biol.* **4**, 483–490 (2008).
52. S. A. Yuzwa *et al.*, Increasing O-GlcNAc slows neurodegeneration and stabilizes tau against aggregation. *Nat. Chem. Biol.* **8**, 393–399 (2012).
53. S. A. Yuzwa, A. H. Cheung, M. Okon, L. P. McIntosh, D. J. Vocadlo, O-GlcNAc modification of tau directly inhibits its aggregation without perturbing the conformational properties of tau monomers. *J. Mol. Biol.* **426**, 1736–1752 (2014).
54. S. Förster *et al.*, Increased O-GlcNAc levels correlate with decreased O-GlcNAcase levels in Alzheimer disease brain. *Biochim. Biophys. Acta* **1842**, 1333–1339 (2014).
55. M. Morris *et al.*, Tau post-translational modifications in wild-type and human amyloid precursor protein transgenic mice. *Nat. Neurosci.* **18**, 1183–1189 (2015).
56. A. Dey *et al.*, Loss of the tumor suppressor BAP1 causes myeloid transformation. *Science* **337**, 1541–1546 (2012).
57. B. J. Winborn *et al.*, The deubiquitinating enzyme ataxin-3, a polyglutamine disease protein, Edits Lys 63 linkages in mixed linkage ubiquitin chains. *J. Biol. Chem.* **283**, 26436–26443 (2008).
58. R.-H. Chen, Y.-H. Chen, T.-Y. Huang, Ubiquitin-mediated regulation of autophagy. *J. Biomed. Sci.* **26**, 80 (2019).
59. J. M. M. Tan *et al.*, Lysine 63-linked ubiquitination promotes the formation and autophagic clearance of protein inclusions associated with neurodegenerative diseases. *Hum. Mol. Genet.* **17**, 431–439 (2008).

60. E. W. Doss-Pepe, E. S. Stenroos, W. G. Johnson, K. Madura, Ataxin-3 interactions with rad23 and valosin-containing protein and its associations with ubiquitin chains and the proteasome are consistent with a role in ubiquitin-mediated proteolysis. *Mol. Cell. Biol.* **23**, 6469–6483 (2003).
61. L. Schöls, P. Bauer, T. Schmidt, T. Schulte, O. Riess, Autosomal dominant cerebellar ataxias: Clinical features, genetics, and pathogenesis. *Lancet Neurol.* **3**, 291–304 (2004).
62. H.-B. Ruan *et al.*, Calcium-dependent O-GlcNAc signaling drives liver autophagy in adaptation to starvation. *Genes Dev.* **31**, 1655–1665 (2017).
63. K. E. Pyo *et al.*, ULK1 O-GlcNAcylation is crucial for activating VPS34 via ATG14L during autophagy initiation. *Cell Rep.* **25**, 2878–2890.e4 (2018).
64. A. Ashkenazi *et al.*, Polyglutamine tracts regulate beclin 1-dependent autophagy. *Nature* **545**, 108–111 (2017).
65. J. Schmidt *et al.*, Vulnerability of frontal brain neurons for the toxicity of expanded ataxin-3. *Hum. Mol. Genet.* **28**, 1463–1473 (2019).
66. S. Hauser *et al.*, Comparative transcriptional profiling of motor neuron disorder-associated genes in various human cell culture models. *Front. Cell Dev. Biol.* **8**, 544043 (2020).
67. S. N. Hayer *et al.*, Generation of an induced pluripotent stem cell line from a patient with spinocerebellar ataxia type 3 (SCA3): HIHCNi002-A. *Stem Cell Res. (Amst.)* **30**, 171–174 (2018).
68. M. W. Pfaffl, A new mathematical model for relative quantification in real-time RT-PCR. *Nucleic Acids Res.* **29**, e45 (2001).